Nano Research

Open Access

Research Article

Trimetallic engineering in MOF-derived catalysts for efficient electrochemical nitrate-to-ammonia conversion

Jiahao Kang[1], Xiaohang Cui[1], Bo Shi[2], Bing Cui[1], Menglan Xiao[1] ✉, and Mingqin Zhao[1] ✉

[1] *Flavors and Fragrance Engineering & Technology Research Center of Henan Province, College of Tobacco Science, Henan Agricultural University, Zhengzhou 450046, China*
[2] *College of Chemistry and Materials Science, Hebei Key Laboratory of Inorganic Nano-materials, Hebei Normal University, Shijiazhuang 050024, China*

Cite this article: *Nano Research*, **2026**, *19*, 94908048. https://doi.org/10.26599/NR.2025.94908048

ABSTRACT: Electrochemical nitrate reduction offers a sustainable route to produce ammonia while simultaneously remediating nitrate pollution. Here, we report a series of trimetallic catalysts derived from carbonized zeolitic imidazolate frameworks (Czif), incorporating Zn and Cu into a Co-based metal-organic framework (MOF) scaffold. Among them, Czif-Zn_3Cu_1 (zinc and copper precursors at a molar ratio of Zn:Cu = 3:1) exhibits the highest Faradaic efficiency (> 90%) and NH_3 yield rate across a broad current density range (100–500 mA/cm^2), outperforming both undoped and bimetallic counterparts. Structural characterization reveals the preservation of MOF morphology, with uniformly dispersed Co, Zn, and Cu sites embedded in a porous N-doped carbon matrix. The optimized Zn:Cu ratio enhances intermediate stabilization and suppresses competing hydrogen evolution, supported by a comprehensive set of analyses. *Operando* flow-cell tests confirm the catalyst's energy efficiency, nitrate tolerance (10–1000 mM), and long-term durability over 100 h. Density functional theory (DFT) calculations confirm that the trimetallic synergy of Czif-Zn_3Cu_1 lowers the overall energy barrier and underpins its enhanced activity. This work highlights the importance of rational trimetallic design and MOF-derived architectures in achieving high-performance electrocatalysts for selective and scalable nitrate-to-ammonia conversion.

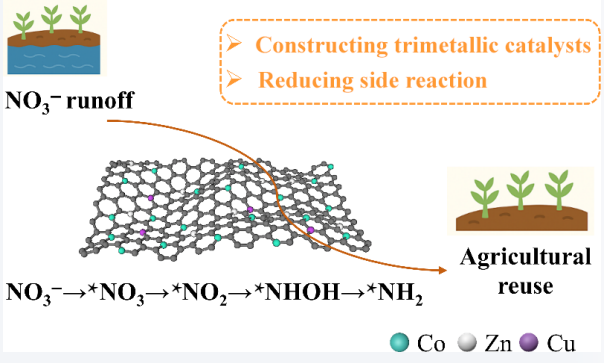

KEYWORDS: nitrate electroreduction, ammonia production, trimetallic engineering, metal-organic framework (MOF)-derived catalysts, synergistic interaction

1 Introduction

Ammonia (NH_3) serves as a cornerstone of the global chemical industry, with applications spanning nitrogen-based fertilizers, pharmaceuticals, and emerging roles in carbon-free energy systems. Current production exceeds 175 million tonnes per year and is projected to rise further with the expansion of food systems and renewable energy integration [1–3]. Industrial ammonia synthesis is currently dominated by the Haber–Bosch process, which operates at elevated temperatures and pressures using hydrogen derived predominantly from fossil fuels [4, 5]. This process is responsible for approximately 2% of global energy consumption and 1.4% of anthropogenic CO_2 emissions, thereby representing a major source of industrial carbon emissions [6].

Concurrently, nitrate pollution has become a pervasive environmental challenge [7]. Excess nitrate, stemming from agricultural runoff and industrial discharge, contaminates groundwater and surface waters worldwide. It contributes to eutrophication and poses serious risks to human health, prompting stringent regulatory limits on drinking water quality [8]. The electrochemical nitrate reduction reaction (NO_3RR) presents a compelling strategy to simultaneously address two pressing challenges: the remediation of nitrate-polluted water resources and the sustainable synthesis of ammonia using renewable electricity [9, 10].

The NO_3RR has attracted increasing attention as a promising alternative to the traditional Haber–Bosch process for ammonia

Received: June 28, 2025; **Revised:** August 18, 2025
Accepted: September 8, 2025

✉Address correspondence to Menglan Xiao, xiaomenglan@henau.edu.cn; Mingqin Zhao, zhaomingqin@126.com

synthesis. Unlike nitrogen reduction, which is hindered by the exceptionally strong N≡N triple bond and suffers from intrinsically sluggish kinetics and poor selectivity, NO_3RR proceeds via multi-electron, proton-coupled transfer steps that bypass the need for N_2 bond activation [11–13]. This enables comparatively lower overpotentials, faster kinetics, and higher product selectivity under ambient conditions. Furthermore, nitrate is highly soluble and readily available in diverse aqueous environments, including industrial wastewater, agricultural runoff, and groundwater, providing an abundant and accessible feedstock. However, the practical implementation of this strategy remains constrained by several factors, including sluggish intermediate transformations, and competing parasitic reactions such as the hydrogen evolution reaction (HER), particularly under alkaline or low-nitrate conditions [14, 15].

Achieving efficient and selective nitrate electroreduction remains a major challenge due to competing HER and incomplete nitrate reduction to intermediates such as NO_2^-. Copper-based catalysts are among the most studied due to their moderate binding affinity for nitrate and favorable energetics for NH_3 formation, yet their performance often falls short at high current densities or under low nitrate concentrations [16, 17]. To overcome these limitations, compositional tuning via bimetallic or trimetallic doping has emerged as an effective strategy. Incorporating additional metal species can modulate the electronic environment, enhance intermediate stabilization, and suppress HER [18–20]. Yu et al. reported that the electronic transport from Zn to Cu promotes the formation of critical intermediates (*CO and *NH_2) and reduces the coupling energy barrier of *CO and *NH_2 [21]. Furthermore, Zn nanoparticles augment the active sites on the electrode surface. The synergistic effect of Cu and Zn is conducive to completely electrochemical remove nitrate [22]. Metal-organic framework (MOF)-derived materials, particularly carbonized zeolitic imidazolate frameworks (Czif), offer a modular platform for constructing such multifunctional catalysts due to their high surface area, tunable composition, and retained porosity post-pyrolysis [23–26].

In this study, we develop a series of trimetallic catalysts derived from Czif, in which copper is doped into a Zn/Co-based scaffold to enhance electrocatalytic nitrate reduction. The resulting Czif-ZnCu materials retain the parent MOF morphology and feature uniformly distributed metal species embedded in a conductive carbon matrix. By tuning the Zn:Cu ratio, we identify Czif-Zn_3Cu_1 as the optimal composition, achieving > 90% Faradaic efficiency (FE) for NH_3 and high yield rates across a broad current density range (100–500 mA·cm^{-2}). The performance enhancement is attributed to the synergistic interaction between Zn and Cu sites, which together promote nitrate activation and suppress competing HER. Czif-Zn_3Cu_1 also demonstrates high nitrate conversion efficiency, robust operation over extended electrolysis, and consistent activity across varying nitrate concentrations. These findings highlight the effectiveness of MOF-derived trimetallic systems in tailoring active sites for selective and scalable NO_3RR, providing a promising strategy for sustainable ammonia synthesis coupled with nitrate remediation.

2 Experimental section

2.1 Materials

All these reagents were of analytical grade and used without further purification. Ethyl alcohol and methanol (AR) were purchased from Tianjin Fuyu Fine Chemical Co., Ltd. $Co(NO_3)_2{\cdot}6H_2O$ (AR, 99%), $Cu(NO_3)_2{\cdot}xH_2O$ (AR), and Zn $(NO_3)_2{\cdot}xH_2O$ (AR, 99%) were obtained from Shanghai Macklin Biochemical Co., Ltd. 2-Methylimidazole (MeIM, 98% purity) was purchased from Energy Chemical.

2.2 Experiment section

Synthesis of Czif. ZIF-67 precursor was synthesized via a facile precipitation method by our previous report [27]. Typically, 3.4930 g of $Co(NO_3)_2{\cdot}6H_2O$ and 3.9408 g of MeIM were added to 100 mL of methanol, respectively. After dissolving, the two solutions were mixed and stirred for 10 min. The obtained solution was kept at ambient temperature for 24 h. The purple precipitate was collected by centrifugation, washed with ethanol, and then dried under vacuum at 60 °C overnight, named ZIF-67. Finally, Czif sample was obtained by calcining ZIF-67 in a N_2 atmosphere at 500 °C for 2 h with a ramp rate of 2 °C/min.

Synthesis of Czif-Zn and Czif-Cu. Various amounts of $Zn(NO_3)_2{\cdot}6H_2O$ and $Co(NO_3)_2{\cdot}6H_2O$ (molar ratio 1:5) were dissolved together in 100 mL of methanol. 3.9408 g of 2-methylimidazole were added to 100 mL of methanol. After dissolving, the two solutions were mixed and stirred for 10 min. Then, the following procedures were same as above. The obtained samples were named Czif-Zn. Similarly, Czif-Cu was prepared the same way as that mentioned above except that $Cu(NO_3)_2{\cdot}xH_2O$ was used as precursors.

Synthesis of Czif-Zn_3Cu_1, Czif-Zn_1Cu_1, and Czif-Zn_1Cu_3. 3.9408 g of $Co(NO_3)_2{\cdot}6H_2O$ was added to 100 mL of methanol. To synthesize samples with different doping amounts, stoichiometric amounts of $Zn(NO_3)_2{\cdot}6H_2O$ and $Cu(NO_3)_2{\cdot}xH_2O$ (in a molar ratio of 3:1, 1:1, and 1:3) were dissolved in above solution. During this process, the molar ratio of (Zn+Cu)/Co was kept at 1/5. 3.9408 g of 2-methylimidazole were added to 100 mL of methanol. Then, the following procedures were same as above. The dried samples were named ZIF-67-Zn_3Cu_1, ZIF-67-Zn_1Cu_1, and ZIF-67-Zn_1Cu_3, respectively. After calcination in N_2 atmosphere, the samples were named Czif-Zn_3Cu_1, Czif-Zn_1Cu_1, and Czif-Zn_1Cu_3, according to the different input quantities.

2.3 Catalyst characterization

In this work, the crystalline structure of catalysts was recorded by a D/max 2500 X-ray powder diffractometer (XRD) with Cu Kα radiation operating in the range of 10°–80° with a scanning rate of 2 °C/min. The morphology of samples was performed on scanning electron microscopy (SEM, Hitachi S-4800), transmission electron microscopy (TEM, HT7700), and high-resolution transmission electron microscopy (HRTEM, JEM-2100F; high-angle annular dark-field scanning transmission electron microscopy (HAADF-STEM), Talos F200S). The surface area, pore volume, and pore size distribution of samples were measured by N_2 adsorption–desorption isotherms at 77 K using an autosorb-iQ instrument, and calculated according to the Brunauer–Emmett–Teller (BET) and Barrett–Joyner–Halenda (BJH) methods. The actual contents of Co, Zn, and Cu were obtained by inductively coupled plasma mass spectrometry (ICP-MS, Thermo iCAP RQ ICP-MS). X-ray photoelectron spectroscope (XPS) was implemented by ESCALAB250XI instrument equipped with Al Kα radiation to investigate the elemental composition and valence states of catalysts.

2.4 Electrochemical measurements

The working electrode was fabricated by spray-coating a catalyst ink onto a hydrophobic carbon paper (SCI Materials Hub Co., Ltd., Anhui, China) [28]. The ink was prepared by dispersing 10 mg of catalyst in a mixture of 250 μL isopropanol, 750 μL deionized water, and 30 μL of 5 wt.% Nafion solution, followed by sonication for 30 min. The resulting suspension was uniformly sprayed onto a 2.5 cm × 2.5 cm hydrophilic carbon paper substrate.

The catalyst-coated carbon paper was employed as the cathode in a membrane electrode assembly (MEA)-based flow electrolyzer, with an active geometric area of 1 cm^2 and a catalyst loading of approximately 2 mg/cm^2 [29, 30]. A nickel foam was used as the anode, and an anion exchange membrane (AEM) was inserted to separate the anolyte and catholyte compartments. Prior to electrolysis, the catalyst was activated by linear sweep voltammetry (LSV). Ammonia production was quantified using ultraviolet–visible (UV–vis) spectrophotometry via the Nessler reagent method after one-hour electrolysis under various constant current densities ranging from 200 to 1000 mA/cm^2.

2.5 Density functional theory (DFT) calculations

We used the DFT as implemented in the Vienna *ab initio* simulation package (VASP) in all calculations. The exchange-correlation potential was described by using the generalized gradient approximation of Perdew–Burke–Ernzerhof (GGA-PBE). The projector augmented-wave (PAW) method was employed to treat interactions between ion cores and valence electrons. The plane-wave cutoff energy was fixed to 450 eV. Given structural models were relaxed until the Hellmann–Feynman forces smaller than −0.02 eV/Å and the change in energy smaller than 10^{-5} eV was attained. Grimme's DFT-D3 methodology was used to describe the dispersion interactions among all the atoms in adsorption models.

The Gibbs free energy change is defined as

$$\Delta G = \Delta E + \Delta \mathrm{ZPE} - T\Delta S$$

where ΔE is the electronic energy calculated with VASP, ΔZPE, and ΔS are the zero-point energy difference and the entropy change between the products and reactants, respectively, and T is the temperature (298.15 K).

3 Results and discussion

3.1 Structural and compositional characterization

Nitrate pollution from agricultural runoff results in nitrate accumulation in water bodies. In Fig. 1(a), through electrochemical reduction powered by renewable electricity, nitrate is converted into NH_3. The produced NH_3 can be further utilized for fertilizer production, enabling agricultural reuse and transforming environmental pollutants into value-added resources [31]. A series of trimetallic catalysts were used for the electrochemical nitrate-to-ammonia conversion. The trimetallic catalysts embedded N-doped carbon framework (denoted as Czif-Zn_xCu_y), using the *in situ* growth of ZIF-67 polyhedrons incorporating Zn and Cu, and followed by pyrolysis of the precursors, as schematically shown in Fig. 1(b).

X-ray diffraction (XRD) pattern of Czif-Zn_3Cu_1 (Fig. S1 in the Electronic Supplementary Material (ESM)) matched well with the simulated ZIF-67 curve, revealing the sodalite structure without additional phases or impurities [32]. In Fig. 1(c), XRD patterns reveal that all Czif-based catalysts exhibit broad peaks, indicative of partially amorphous carbon matrices with embedded crystalline phases. The undoped Czif sample shows a weak peak at ~ 44.2°, assigned to metallic Co(111), while the Zn- and Cu-containing samples display additional peaks at ~ 36.5° and ~ 42.4°, corresponding to CoO(111) and CoO(200), respectively. These results suggest that heteroatom doping promotes partial oxidation

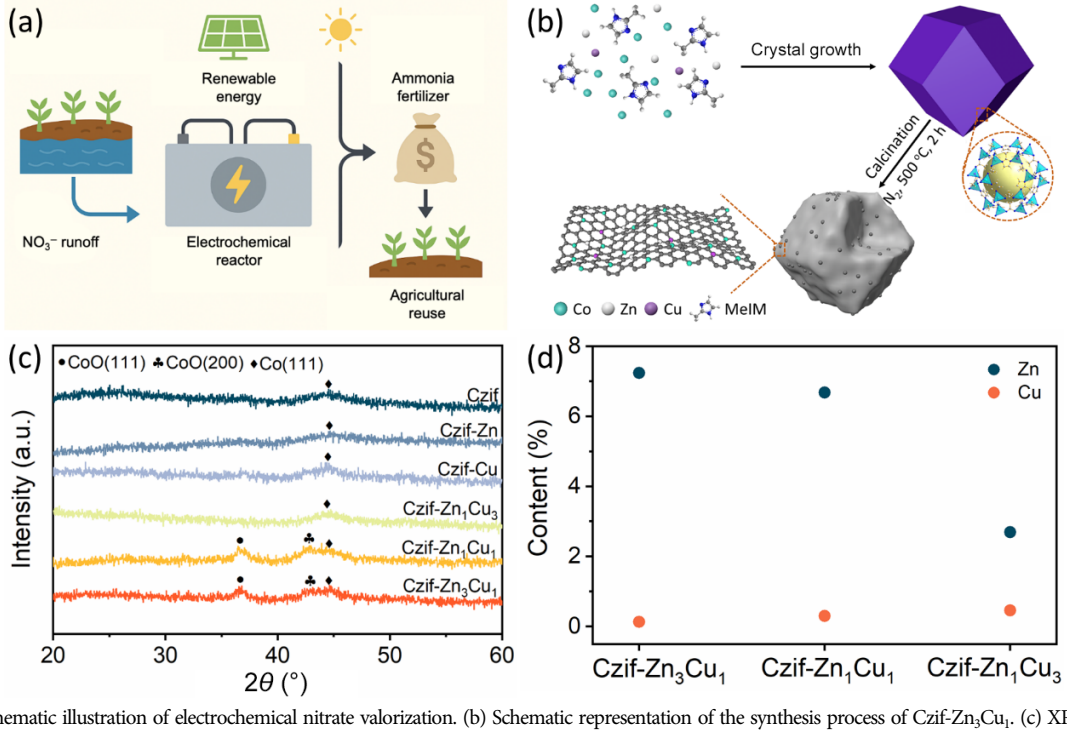

Figure 1 (a) Schematic illustration of electrochemical nitrate valorization. (b) Schematic representation of the synthesis process of Czif-Zn_3Cu_1. (c) XRD patterns of all samples. (d) The content of Zn and Cu measured by ICP-MS.

of cobalt during pyrolysis. Furthermore, the peaks of Co(111) plane slightly weaken after the introduction of Cu and Zn. It is likely that the impregnation of Cu^{2+} and Zn^{2+} into ZIF-67 distort the lattice structure of ZIF-67 crystals due to the interactions between metal ions and MeIM organic linkers [33]. No distinct reflections from Zn or Cu phases are observed, likely due to their low concentration or high dispersion. This is supported by ICP-MS results (Fig. 1(d)), which confirm successful incorporation of Zn and Cu with tunable ratios. Czif-Zn_3Cu_1 contains the highest Zn content (7.23%) and lowest Cu (0.13%), whereas Czif-Zn_1Cu_3 exhibits the highest Cu content (0.46%) and lowest Zn (2.69%). The detailed contents of all metals list in Table S1 in the ESM. These variations reflect controllable metal loading through precursor stoichiometry.

The morphological evolution of catalysts was characterized using SEM and TEM. Prior to pyrolysis, the ZIF-derived precursors exhibit well-defined rhombic dodecahedral structures with smooth surfaces, typical of ZIF-67 crystallites (Figs. S2 and S3 in the ESM). After pyrolysis, the overall polyhedral framework of Czif-derived catalysts is preserved, but the surface becomes rougher and more porous, suggesting partial collapse and carbonization of the MOF skeleton (Figs. 2(a) and 2(c)). In Fig. 2(b), TEM images of Czif confirm the uniform polyhedral morphology with ca. 720 nm in diameter, in which embedded nanoparticles averaging 5.1 ± 1.3 nm. Figure 2(d) shows that Czif-Zn_3Cu_1 sample exhibits a polyhedron with a size of ca. 630 nm. The average particle size in Czif-Zn_3Cu_1 increases to 6.8 ± 1.4 nm, maybe due to the expansion of the lattice after the incorporation of Zn and Cu.

High-resolution TEM reveals well-resolved lattice fringes with interplanar spacings of 0.246 and 0.208 nm, corresponding to the (111) planes of CoO and metallic Co, respectively (Fig. 2(e) and Fig. S4 in the ESM). The coexistence of crystalline Co and CoO domains within the carbon matrix suggests partial reduction of cobalt species during pyrolysis, consistent with the XRD observations. Additionally, the presence of graphitic carbon layers is visible, which may enhance electrical conductivity and structural stability of the catalyst [34]. STEM-energy dispersive spectroscopy (EDS) elemental mappings of Czif-Zn_3Cu_1 in Fig. 2(f) show the distribution of Co, Zn, and Cu. A trimetallic architecture comprising Co nanoclusters embedded in N-doped carbon, in conjunction with highly dispersed Zn–N_x and Cu–N_x coordination sites was obtained, suggesting a well-integrated composite structure. The compositional uniformity and compactness confirmed the formation of active sites, which is conducive to the transfer of electrons between metals. These results demonstrate that the pyrolysis process effectively transforms the MOF precursor into a porous, conductive carbon-metal composite, while preserving the desirable morphology and generating nanoscale catalytic domains.

3.2 Physical properties and surface chemical states

The specific surface area and porosity of the Czif-based catalysts were analyzed by N_2 adsorption–desorption isotherms. In Fig. 3(a), all samples exhibit type-IV isotherms with H3-type hysteresis loops, indicative of mesoporous structures. The specific surface areas increase upon Zn and Cu doping: Czif-Zn_3Cu_1 reaches 70.9 m^2/g, followed by Czif-Zn_1Cu_3 (60.4 m^2/g), both higher than the undoped Czif (52.8 m^2/g). Pore size distribution data of samples are shown in Fig. 3(b) and Table S2 in the ESM. All samples display similar average pore sizes of ~ 3.84 nm, indicating mesoporosity is retained after pyrolysis. Interestingly, while the total pore volume of Czif-Zn_3Cu_1 (0.10 cm^3/g) is slightly lower than that of Czif (0.11 cm^3/g), its increased surface area suggests a higher density of accessible mesopores, which can benefit mass transport and catalytic turnover.

XPS was employed to probe the surface composition and electronic environments of the catalysts. The survey spectra (Fig. 3(c)) confirm the presence of Co, Zn, Cu, C, N, and O species. High-resolution N 1s spectra (Fig. 3(d)) reveal multiple nitrogen species, which could be divided into four peaks at about 398.2,

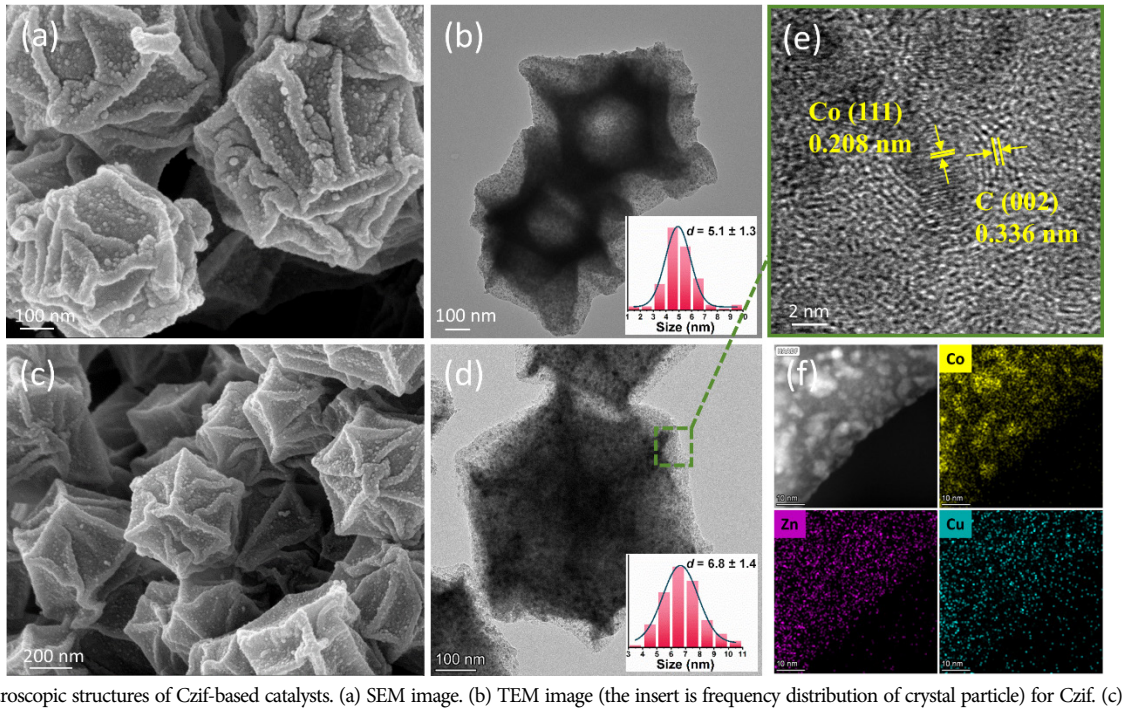

Figure 2 Microscopic structures of Czif-based catalysts. (a) SEM image. (b) TEM image (the insert is frequency distribution of crystal particle) for Czif. (c) SEM image. (d) TEM image (the inset is frequency distribution of crystal particle). (e) HRTEM image for Czif-Zn_3Cu_1. (f) HAADF-STEM image and the corresponding STEM-EDS elemental mappings of Czif-Zn_3Cu_1.

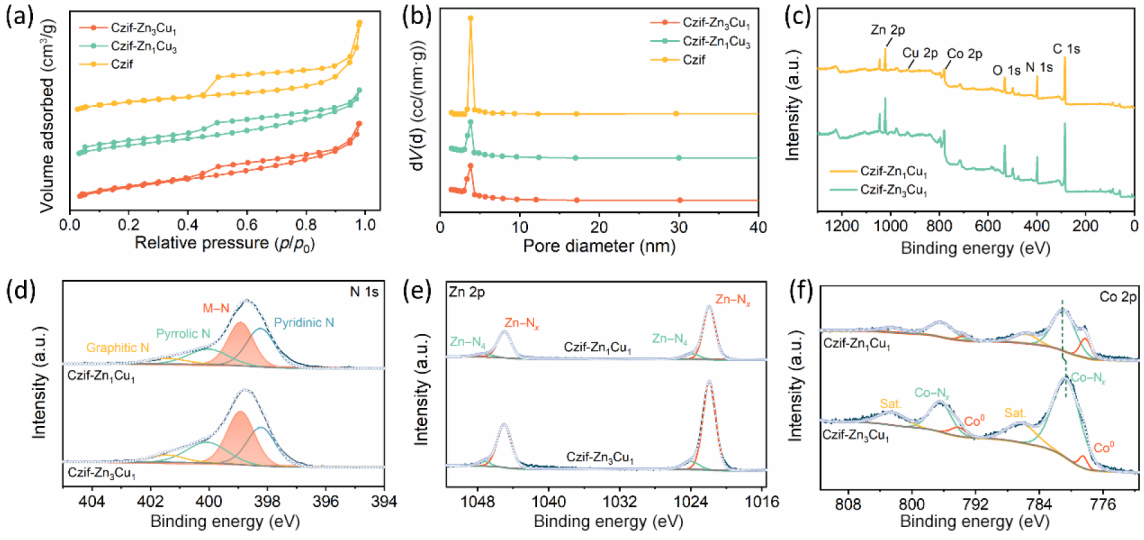

Figure 3 Physical properties and surface chemical states of Czif-based catalysts. (a) Nitrogen adsorption–desorption isotherms and (b) corresponding pore size distribution curves for Czif, Czif-Zn_1Cu_3, and Czif-Zn_3Cu_1, showing mesoporous structures and enhanced surface area upon bimetallic doping. (c) XPS survey spectra confirming the presence of Zn, Cu, Co, C, N, and O elements. (d) High-resolution N 1s spectra deconvoluted into pyridinic N, pyrrolic N, graphitic N, and M–N species. (e) Zn 2p spectra showing dominant Zn–N_x and Zn–N_4 coordination environments. (f) Co 2p spectra fitted to Co^0, Co–N_x, and satellite peaks.

398.9, 400.1, and 401.4 eV, in accordance with pyridinic N, metal-coordinated N (M–N), pyrrolic N, and graphitic N, respectively [35]. As previously reported, pyridinic N, with its lone pair of electrons, which could act as electron donors, facilitate the adsorption of nitrate anions through electrostatic interactions [36, 37]. The M–N sites can directly participate in the activation of nitrate molecules. The metal center in the M–N complex can attract the oxygen atoms of nitrate ions through its positive charge, while the coordinated N can influence the electron density around the metal, thereby weakening the N=O bonds in nitrate [38]. In Table S3 in the ESM, Czif-Zn_3Cu_1 exhibits a higher proportion of M–N and pyridinic N, which are conducive to promoting the nitrate reduction.

The Zn 2p spectra (Fig. 3(e)) could be deconvoluted into four peaks, in which the peaks at 1021.8 and 1044.9 eV are attributed to Zn–N_x, and other peaks are assigned to Zn–N_4, indicating successful integration into the N-doped carbon matrix [33]. Furthermore, Zn LMM Auger electron spectra (Fig. S5 in the ESM) confirm that Zn species is in a highly coordinated environment, rather than close to the metallic state. Cu signals are weak due to low concentration, but their incorporation is supported by ICP data (Fig. S6 in the ESM). In Fig. 3(f), two distinct peaks at ca.780.6 (Co $2p_{3/2}$) and 796.5 eV (Co $2p_{1/2}$) are observed in Co 2p spectra. The deconvolution of Co $2p_{3/2}$ spectra further reveal that all samples mainly consist of two peaks at ca. 778.5 and 780.6 eV, corresponding to metallic state Co^0 and Co–N_x coordination structure, accompanied by a satellite peak. For the Co $2p_{1/2}$ peak, Co^0, Co–N_x, and satellite peaks are located at 794.2, 796.4, and 802.4 eV, respectively [39, 40]. The presence of Co–N_x suggests the formation of atomically dispersed Co sites [41]. The offset of binding energy in electron spectra demonstrates that co-doping with Zn and Cu tunes the surface electronic structure and chemical environment of the catalysts, conducive to the formation of trimetallic catalysts. Thus, the abundant accessible metal-nitrogen active sites could enhance electrochemical functionality.

3.3 Electrocatalytic nitrate reduction performance

The electrocatalytic nitrate reduction performance of the Czif-based catalysts was systematically evaluated in a MEA flow electrolyzer under industrially relevant current densities (Fig. 4(a)). Among the series, Czif-Zn_3Cu_1 exhibited superior NH_3 selectivity, yield rate, and long-term stability across various operating conditions.

In flow-cell experiments, Czif-Zn_3Cu_1 exhibited the most favorable electrocatalytic performance among all tested catalysts. It achieved a FE for NH_3 exceeding 90% at 100 mA/cm² and sustained high efficiency across a broad current density window (100–500 mA/cm²), substantially outperforming both the undoped Czif and other bimetallic counterparts (Figs. 4(b) and 4(c)). This superior selectivity suggests that the optimized Zn:Cu ratio in Czif-Zn_3Cu_1 promotes a favorable surface electronic structure that enhances nitrate adsorption and activation while effectively suppressing the competing HER. Correspondingly, the NH_3 yield rate increased proportionally with current density, reaching a maximum of ~ 18 mg/(h·cm²) at 500 mA/cm², an indication of its strong catalytic turnover under industrially relevant conditions (Fig. 4(d)).

Furthermore, Czif-Zn_3Cu_1 demonstrated the lowest operating cell voltages (E_{cell}) at all tested current densities (Fig. 4(e)), confirming its superior energy efficiency. This reduced overpotential can be attributed to the synergistic electronic effects between Co, Zn, and Cu active centers and the highly conductive carbon framework, which together facilitate charge transfer and reduce kinetic barriers for intermediate transformation.

The catalyst also exhibited remarkable tolerance to varying nitrate concentrations, maintaining > 85% FE even at low nitrate levels (10 mM) and up to 1000 mM (Fig. 4(f)), indicating its potential suitability for both wastewater treatment and concentrated nitrate sources. Time-resolved electrolysis further revealed a progressive and near-complete NO_3^- removal (~ 95%) within 120 min (Fig. 4(g)), showcasing the material's rapid and efficient denitrification capability. Finally, long-term stability testing under constant current (100 mA cm⁻²) confirmed excellent operational durability, with E_{cell} and FE remaining unchanged over a 100-hour period (Fig. 4(h)), highlighting the mechanical robustness and chemical resilience of the catalyst in continuous flow operation.

The enhanced activity of Czif-Zn_3Cu_1 can be attributed to the

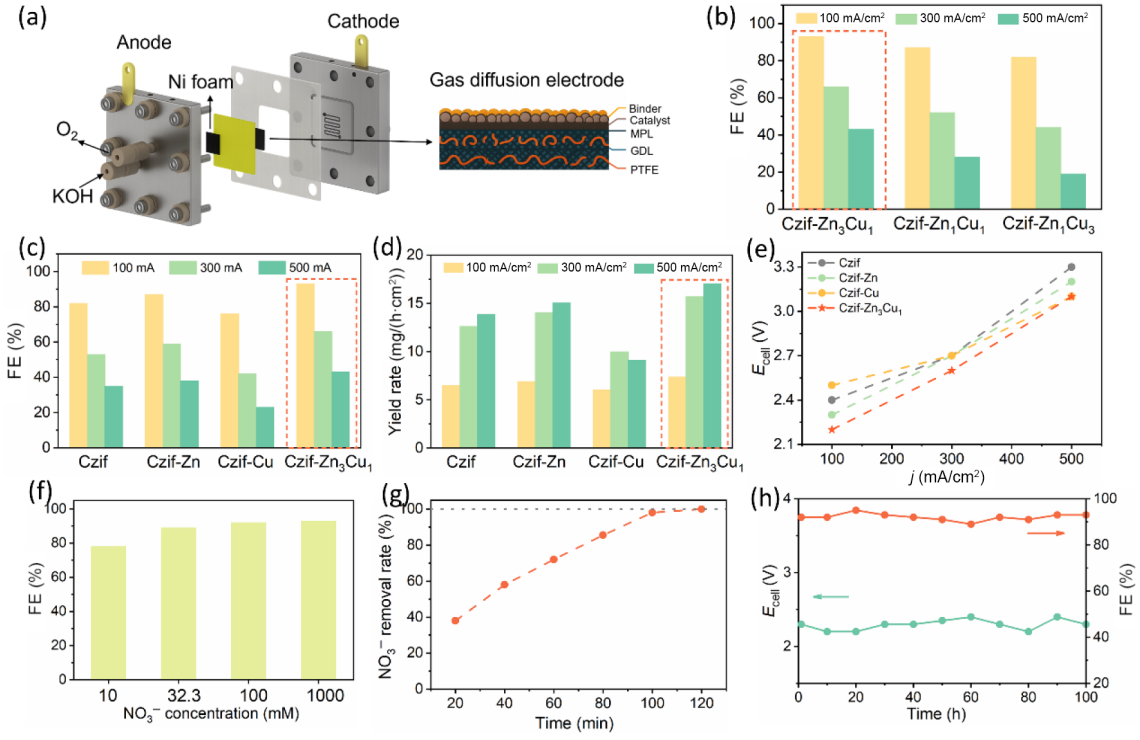

Figure 4 Electrocatalytic nitrate reduction performance of Czif-based catalysts in a flow cell system. (a) Schematic of the MEA-based flow electrolyzer and gas diffusion electrode configuration. (b) FE for NH_3 production at different current densities (100, 300, and 500 mA/cm^2) for Czif, Czif-Zn, Czif-Cu, and Czif-Zn_3Cu_1. (c) FE comparison among Czif-Zn_3Cu_1, Czif-Zn_1Cu_1, and Czif-Zn_1Cu_3 under varying current densities. (d) NH_3 yield rates of all catalysts at different current densities. (e) Corresponding E_{cell} versus current density curves, highlighting improved energy efficiency of Czif-Zn_3Cu_1. (f) FE of Czif-Zn_3Cu_1 at different NO_3^- concentrations (10–1000 mM). (g) Time-dependent NO_3^- removal rate by Czif- Zn_3Cu_1 at 100 mA/cm^2. (h) Long-term stability test of Czif-Zn_3Cu_1 over 100 h, showing consistent E_{cell} and FE for NH_3.

optimized interplay between composition, structure, and electronic environment. ICP-MS data confirmed successful incorporation of Cu and Zn in controlled ratios, with Czif-Zn_3Cu_1 containing the highest Zn content and moderate Cu content (0.13%), enabling a synergistic balance between nitrate activation and hydrogen evolution suppression. XRD and HRTEM analyses revealed the coexistence of Co and CoO phases embedded in a conductive carbon matrix, suggesting that partial oxidation of cobalt may further facilitate electron transfer and intermediate stabilization. BET analyses indicated that Czif-Zn_3Cu_1 possessed the highest specific surface area (70.9 m^2/g), with consistent mesopore size (~ 3.84 nm). Such mesoporosity, combined with higher surface area, likely improves electrolyte access and accelerates mass transport, contributing to higher catalytic turnover.

XPS results further support the formation of catalytically active nitrogen-coordinated metal sites. In particular, Czif-Zn_3Cu_1 exhibited a higher proportion of pyridinic N and M–N_x species, which are known to facilitate nitrate adsorption and multielectron reduction pathways. The presence of Co–N_x and Zn–N_x coordination motifs suggests the formation of atomically dispersed active sites capable of stabilizing intermediates such as NO_2^- and NH_2OH during the reduction sequence.

These results collectively suggest that Cu doping at an optimal Zn:Cu ratio improves both catalytic selectivity and energetic efficiency by tuning the local coordination environment, modifying electronic structure, and increasing accessible active surface area. The use of a MOF-derived architecture ensures well-dispersed active sites within a hierarchically porous, conductive matrix—critical for high-rate electrocatalysis.

3.4 Mechanistic insight into the synergistic role

The proposed mechanism in Fig. 5, supported by DFT free-energy calculations, illustrates the structural and electronic origins of the superior nitrate reduction activity of Czif-Zn_3Cu_1. In comparison to Czif-Cu, Czif-Zn_3Cu_1 exhibits a significantly lower potential-determining step (PDS) energy barrier (–0.376 vs. –0.249 eV), indicating more favorable energetics for the conversion of *NO to *NHO. This reduction in barrier energy stems from the optimized Zn:Cu ratio. Zn incorporation strengthens the adsorption of nitrate and stabilizes key intermediates (*NO_2, *NO), while trace Cu dopants modulate the electronic structure to suppress parasitic hydrogen evolution and promote charge redistribution at the active sites. The coexistence of Co–N_x, Zn–N_x, and Cu–N_x coordination motifs thus generates a multifunctional catalytic interface that effectively stabilizes intermediates, leading to a smoother free-energy landscape for ammonia formation. In addition, the

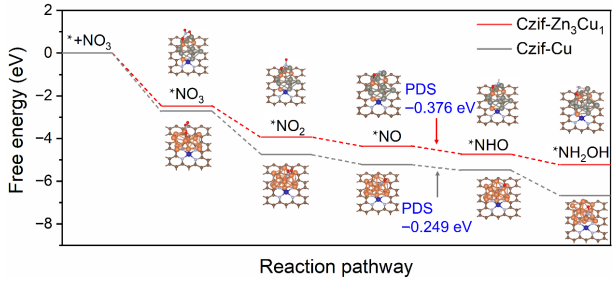

Figure 5 The calculated NO_3RR Gibbs free energy diagrams over Czif-Cu and Czif-Zn_3Cu_1. Atom color-coding: indigo, cobalt; blue, nitrogen; orange, copper; gray, zinc; red, oxygen; white, hydrogen.

preserved mesoporous architecture derived from the MOF precursor ensures efficient mass transport, further supporting high-rate nitrate reduction. Collectively, the DFT calculations and structural analyses confirm that the trimetallic synergy of Czif-Zn_3Cu_1 lowers the overall energy barrier and underpins its enhanced activity, selectivity, and stability for NO_3RR.

4 Conclusion

In summary, we have developed a trimetallic electrocatalyst (Czif-Zn_3Cu_1) derived from a Co-based MOF precursor, exhibiting outstanding performance for electrochemical nitrate reduction. The optimized composition leverages the synergistic roles of Zn and Cu: Zn promotes nitrate adsorption and intermediate stabilization, while trace Cu content suppresses hydrogen evolution and modulates the local electronic environment. Structural analyses confirm the preservation of MOF morphology, formation of mesoporous carbon frameworks, and abundant Co–N_4, Zn–N_x, and Cu–N_x active sites. Electrochemical tests demonstrate > 90% NH_3 Faradaic efficiency, high yield rates under industrially relevant current densities, and operational stability over 100 h. DFT calculations verify that the trimetallic synergy in Czif-Zn_3Cu_1 reduces the overall energy barrier, thereby supporting its improved activity, selectivity, and stability in NO_3RR. The catalyst also maintains high efficiency across a wide range of nitrate concentrations, indicating broad applicability for both wastewater treatment and sustainable ammonia synthesis. This study offers valuable insights into compositional engineering strategies using MOF-derived systems, and paves the way toward practical electrochemical nitrogen-cycle technologies.

Electronic Supplementary Material: Supplementary material (XRD pattern of ZIF-67-Zn_3Cu_1; SEM and TEM images of ZIF-67-Zn_3Cu_1; Zn LMM Auger electron spectra, XPS spectra of Cu 2p for Czif-67-Zn_1Cu_1 and Czif-67-Zn_3Cu_1; the content of metals determined by ICP; textural parameters of all catalysts derived from N_2 physisorption results; surface chemical composition and elemental molar ratio of as-prepared catalysts) is available in the online version of this article at https://doi.org/10.26599/NR.2025.94908048.

Data availability

All data needed to support the conclusions in the paper are presented in the manuscript and the Electronic Supplementary Material. Additional data related to this paper may be requested from the corresponding author upon request.

Acknowledgements

This work was supported by the National Natural Science Foundation of China (No. 22406049) and China Postdoctoral Science Foundation (No. GZC20240432).

Declaration of competing interest

All the contributing authors report no conflict of interests in this work.

Author contribution statement

J. H. K.: Data curation, writing manuscript, experimental design. X. H. C.: Data curation, validation, experimental design. B. S.: Validation, data curation. B. C.: Project administration,validation. M. L. X.: Funding acquisition, writing manuscript. M. Q. Z.: Project administration, funding acquisition. All the authors have approved the final manuscript.

Use of AI statement

None.

References

[1] Zhang, H. R.; Wang, H. J.; Cao, X. Q.; Chen, M. S.; Liu, Y. L.; Zhou, Y. T.; Huang, M.; Xia, L.; Wang, Y.; Li, T. S. et al. Unveiling cutting-edge developments in electrocatalytic nitrate-to-ammonia conversion. *Adv. Mater.* **2024**, *36*, 2312746.

[2] Hu, J.; Huang, H.; Yu, M.; Wang, S.; Li, J. P. Electron engineering of nickel phosphide for $Ni^{\delta+}$ in electrochemical nitrate reduction to ammonia. *Nano Res.* **2024**, *17*, 4864–4871.

[3] Ma, G.; Liu, W. X.; Li, S. S.; Zhang, P. P.; Wang, C. Y.; Lu, H. F.; Wang, L. F.; Xie, Y. X.; Ma, D. Y.; Kang, G. Z. Determining the optimal N input to improve grain yield and quality in winter wheat with reduced apparent N loss in the North China plain. *Front. Plant Sci.* **2019**, *10*, 181.

[4] Chen, J. G.; Crooks, R. M.; Seefeldt, L. C.; Bren, K. L.; Bullock, R. M.; Darensbourg, M. Y.; Holland, P. L.; Hoffman, B.; Janik, M. J.; Jones, A. K. et al. Beyond fossil fuel-driven nitrogen transformations. *Science* **2018**, *360*, eaar6611.

[5] Martín, A. J.; Shinagawa, T.; Pérez-Ramírez, J. Electrocatalytic reduction of nitrogen: From haber-bosch to ammonia artificial leaf. *Chem* **2019**, *5*, 263–283.

[6] Wang, J.; Cai, C.; Wang, Y. A.; Yang, X. M.; Wu, D. J.; Zhu, Y. M.; Li, M. H.; Gu, M.; Shao, M. H. Electrocatalytic reduction of nitrate to ammonia on low-cost ultrathin CoO_x nanosheets. *ACS Catal.* **2021**, *11*, 15135–15140.

[7] Zhu, P.; Li, S. Z.; Qin, J. Z.; Zhu, J. M.; Li, J.; Zuo, K. C.; Zhao, H. Z.; Zhang, Z. B. Enhanced electrochemical deuterated ammonia (ND_3) production via microenvironment-regulated nitrate reduction. *Adv. Energy Mater.*, in press, https://doi.org/10.1002/aenm.202502344.

[8] Clark, R. M.; Ehreth, D. J.; Convery, J. J. Water legislation in the U.S.: An overview of the safe drinking water act. *Toxicol. Ind. Health* **1991**, *7*, 43–52.

[9] Xu, H.; Ma, Y. Y.; Chen, J.; Zhang, W. X.; Yang, J. P. Electrocatalytic reduction of nitrate—A step towards a sustainable nitrogen cycle. *Chem. Soc. Rev.* **2022**, *51*, 2710–2758.

[10] Xiong, Y. C.; Wang, Y. H.; Zhou, J. W.; Liu, F.; Hao, F. K.; Fan, Z. X. Electrochemical nitrate reduction: Ammonia synthesis and the beyond. *Adv. Mater.* **2024**, *36*, 2304021.

[11] Skúlason, E.; Bligaard, T.; Gudmundsdóttir, S.; Studt, F.; Rossmeisl, J.; Abild-Pedersen, F.; Vegge, T.; Jónsson, H.; Nørskov, J. K. A theoretical evaluation of possible transition metal electro-catalysts for N_2reduction. *Phys. Chem. Chem. Phys.* **2012**, *14*, 1235–1245.

[12] Wang, J. Q.; Jiang, Z.; Peng, G. M.; Hoenig, E.; Yan, G. B.; Wang, M. Z.; Liu, Y. Y.; Du, X. W.; Liu, C. Surface valence state effect of MoO_{2+x} on electrochemical nitrogen reduction. *Adv. Sci.* **2022**, *9*, 2104857.

[13] Fan, X. Y.; Liu, C. Z.; Li, Z. X.; Cai, Z. W.; Ouyang, L.; Li, Z. R.; He, X.; Luo, Y. S.; Zheng, D. D.; Sun, S. J. et al. Pd-doped Co_3O_4 nanoarray for efficient eight-electron nitrate electrocatalytic reduction to ammonia synthesis. *Small* **2023**, *19*, 2303424.

[14] Zhou, J.; Wen, M.; Huang, R.; Wu, Q. S.; Luo, Y. X.; Tian, Y. K.; Wei, G. F.; Fu, Y. Q. Regulating active hydrogen adsorbed on grain boundary defects of nano-nickel for boosting ammonia electrosynthesis from nitrate. *Energy Environ. Sci.* **2023**, *16*, 2611–2620.

[15] Foster, S. L.; Bakovic, S. I. P.; Duda, R. D.; Maheshwari, S.; Milton, R. D.; Minteer, S. D.; Janik, M. J.; Renner, J. N.; Greenlee, L. F. Catalysts for nitrogen reduction to ammonia. *Nat. Catal.* **2018**, *1*, 490–500.

[16] Wang, Y. T.; Zhou, W.; Jia, R. R.; Yu, Y. F.; Zhang, B. Unveiling the activity origin of a copper-based electrocatalyst for selective nitrate reduction to ammonia. *Angew. Chem., Int. Ed.* **2020**, *59*, 5350–5354.

[17] Wu, K. M.; Sun, C. C.; Wang, Z. N.; Song, Q.; Bai, X. X.; Yu, X.; Li, Q.; Wang, Z.; Zhang, H.; Zhang, J. et al. Surface reconstruction on uniform Cu nanodisks boosted electrochemical nitrate reduction to ammonia. *ACS Mater. Lett.* **2022**, *4*, 650–656.

[18] Xiao, C. H.; Guo, Y. X.; Sun, J. Y.; Guo, T.; Jia, X. Y.; Guo, S. N.; Wu, G. C.; Sun, Y.; Yao, Z. Y.; Liu, Y. Efficient electrocatalytic reduction of nitrate to ammonia at low concentration by copper-cobalt oxide nanowires with shell–core structure. *Nano Res.* **2024**, *17*, 5087–5094.

[19] Zhang, S.; Wu, J. H.; Zheng, M. T.; Jin, X.; Shen, Z. H.; Li, Z. H.; Wang, Y. J.; Wang, Q.; Wang, X. B.; Wei, H. et al. Fe/Cu diatomic catalysts for electrochemical nitrate reduction to ammonia. *Nat. Commun.* **2023**, *14*, 3634.

[20] He, W. H.; Zhang, J.; Dieckhöfer, S.; Varhade, S.; Brix, A. C.; Lielpetere, A.; Seisel, S.; Junqueira, J. R. C.; Schuhmann, W. Splicing the active phases of copper/cobalt-based catalysts achieves high-rate tandem electroreduction of nitrate to ammonia. *Nat. Commun.* **2022**, *13*, 1129.

[21] Meng, N. N.; Ma, X. M.; Wang, C. H.; Wang, Y. T.; Yang, R.; Shao, J.; Huang, Y. M.; Xu, Y.; Zhang, B.; Yu, Y. F. Oxide-derived core–shell Cu@Zn nanowires for urea electrosynthesis from carbon dioxide and nitrate in water. *ACS Nano* **2022**, *16*, 9095–9104.

[22] Wang, L. L.; Lv, X. F.; Geng, P. H.; Wang, Z. K.; Sun, J. H. Cu and Zn metal particles modified nanocathode based electrocatalytic nitrate reduction: Effective, selective and mechanism. *J. Electroanal. Chem.* **2024**, *954*, 118053.

[23] Zhang, J.; Zeng, H. X.; Bu, L. J.; Zhou, S. Q.; Shi, Z.; Deng, L. Cu^0 incorporated cobalt/nitrogen doped carbonaceous frameworks derived from ZIF-67 (Cu@Co-N-C) as PMS activator for efficient degradation of naproxen: Direct electron transfer and $^1O_2$ dominated nonradical mechanisms. *Chem. Eng. J.* **2023**, *454*, 139989.

[24] Kuang, M.; Wang, Q. H.; Han, P.; Zheng, G. F. Cu, Co-embedded N-enriched mesoporous carbon for efficient oxygen reduction and hydrogen evolution reactions. *Adv. Energy Mater.* **2017**, *7*, 1700193.

[25] Duan, C. X.; Yu, Y.; Hu, H. Recent progress on synthesis of ZIF-67-based materials and their application to heterogeneous catalysis. *Green Energy Environ.* **2022**, *7*, 3–15.

[26] Guo, C. Y.; Shen, L. Y.; Tang, Y. J.; Ciucci, F.; Tang, Z. H. Cu nanowires encapsulated by ZIF67 for efficient ammonia electrosynthesis from nitrate. *ChemSusChem* **2025**, *18*, e202401418.

[27] Xiao, M. L.; Yu, X. L.; Guo, Y. C.; Ge, M. F. Boosting toluene combustion by tuning electronic metal-support interactions in *in situ* grown Pt@Co_3O_4 catalysts. *Environ. Sci. Technol.* **2022**, *56*, 1376–1385.

[28] Wang, J. D.; Zhu, P.; Qin, H. L.; Zuo, K. C.; Zhao, H. Z.; Zhang, Z. B. Electrochemical reactors for the utilization of liquid-phase carbon species. *Energy Environ. Sci.* **2025**, *18*, 6438–6455.

[29] Zhang, Z. B. Low-temperature electrochemical cement clinker production. *ACS Energy Lett.* **2023**, *8*, 3927–3934.

[30] Meng, F. X.; Qin, J. Z.; Wu, Q. H.; Dai, H. W.; Zhu, P.; Tang, T.; Zhang, L. X.; Zhang, Z. B.; Zuo, K. C. Identifying the critical oxygenated functional groups on graphene oxide for efficient water dissociation in bipolar membranes. *ACS Energy Lett.* **2024**, *9*, 5444–5451.

[31] Ishaq, H.; Crawford, C. Review of ammonia production and utilization: Enabling clean energy transition and net-zero climate targets. *Energy Convers. Manage.* **2024**, *300*, 117869.

[32] Han, D. W.; Ma, X. Y.; Yang, X. Q.; Xiao, M. L.; Sun, H.; Ma, L. J.; Yu, X. L.; Ge, M. F. Metal organic framework-templated fabrication of exposed surface defect-enriched Co_3O_4 catalysts for efficient toluene oxidation. *J. Colloid Interface Sci.* **2021**, *603*, 695–705.

[33] Budi, C. S.; Deka, J. R.; Hsu, W. C.; Saikia, D.; Chen, K. T.; Kao, H. M.; Yang, Y. C. Bimetallic Co/Zn zeolitic imidazolate framework ZIF-67 supported Cu nanoparticles: An excellent catalyst for reduction of synthetic dyes and nitroarenes. *J. Hazard. Mater.* **2021**, *407*, 124392.

[34] Lu, C.; Chen, X. Nanostructure engineering of graphitic carbon nitride for electrochemical applications. *ACS Nano* **2021**, *15*, 18777–18793.

[35] Gao, Y. N.; Han, Z. S.; Hong, S.; Wu, T. B.; Li, X.; Qiu, J. S.; Sun, Z. Y. ZIF-67-derived cobalt/nitrogen-doped carbon composites for efficient electrocatalytic N_2 reduction. *ACS Appl. Energy Mater.* **2019**, *2*, 6071–6077.

[36] Wang, X. R.; Liu, J. Y.; Liu, Z. W.; Wang, W. C.; Luo, J.; Han, X. P.; Du, X. W.; Qiao, S. Z.; Yang, J. Identifying the key role of pyridinic-N–Co bonding in synergistic electrocatalysis for reversible ORR/OER. *Adv. Mater.* **2018**, *30*, 1800005.

[37] Marshall-Roth, T.; Libretto, N. J.; Wrobel, A. T.; Anderton, K. J.; Pegis, M. L.; Ricke, N. D.; van Voorhis, T.; Miller, J. T.; Surendranath, Y. A pyridinic Fe–N_4 macrocycle models the active sites in Fe/N-doped carbon electrocatalysts. *Nat. Commun.* **2020**, *11*, 5283.

[38] Liu, J. J.; Gong, Z. C.; Allen, C.; Ge, W.; Gong, H. S.; Liao, J. W.; Liu, J. B.; Huang, K.; Yan, M. M.; Liu, R. et al. Edge-hosted Fe-N_3 sites on a multiscale porous carbon framework combining high intrinsic activity with efficient mass transport for oxygen reduction. *Chem Catal.* **2021**, *1*, 1291–1307.

[39] Zhang, J. J.; Liu, W.; He, F.; Song, M.; Huang, X.; Shen, T.; Li, J. W.; Zhang, C.; Zhang, J.; Wang, D. L. Highly dispersed Co atoms anchored in porous nitrogen-doped carbon for acidic H_2O_2 electrosynthesis. *Chem. Eng. J.* **2022**, *438*, 135619.

[40] Wang, D.; Yuan, M. W.; Xu, J. S.; Li, Y. Y.; Shi, K. F.; Yang, H.; Li, H. F.; Sun, G. B. Highly active atomically dispersed Co–N_x sites anchored on ultrathin N-doped carbon nanosheets with durability oxygen reduction reaction of zinc-air batteries. *ACS Sustainable Chem. Eng.* **2021**, *9*, 16956–16964.

[41] Yu, N. F.; Chen, H.; Kuang, J. B.; Bao, K. L.; Yan, W.; Ye, J. L.; Yang, Z. T.; Huang, Q. H.; Wu, Y. P.; Sun, S. G. Efficient oxygen electrocatalysts with highly-exposed Co–N_4 active sites on N-doped graphene-like hierarchically porous carbon nanosheets enhancing the performance of rechargeable Zn-air batteries. *Nano Res.* **2022**, *15*, 7209–7219.